A.M. Mitchell, P. Panicucci, V. Franzese, F. Topputo, R. Linares
Improved Detection of a Near-Earth Asteroid from an Interplanetary CubeSat Mission
Acta Astronautica, published online 27/07/2024
doi:10.1016/j.actaastro.2024.07.010

Improved Detection of a Near-Earth Asteroid from an Interplanetary CubeSat Mission

Adriana M. Mitchell[a], Paolo Panicucci[b], Vittorio Franzese[b], Francesco Topputo[b], Richard Linares[a]

[a]*Department of Aeronautics and Astronautics, MIT, 77 Massachusetts Ave, Cambridge, 02139, MA, USA*
[b]*Department of Aerospace Science and Technology, Politecnico di Milano, Via La Masa, 34, 20156, Milano, Italy*

Abstract

This study focuses on the autonomous detection of small (diameter < 50 m) faint (absolute magnitude > 20) Near-Earth Asteroids (NEAs) using commercial off-the-shelf (COTS) cameras during the approach phase of interplanetary CubeSat missions. To address the challenge of low signal-to-noise ratio (SNR) in COTS CubeSat sensors, a design tool was developed that incorporates camera parameters, asteroid parameters, approach phase geometry and an Earth-observation based SNR boosting technique, to ensure the autonomous detection of small NEAs during the approach phase. The tool generates a synthetic SNR that meets the target asteroid detection requirements (SNR ≥ 7) by stacking multiple frames of the target asteroid. The design tool defines requirements at the camera and trajectory design levels, exploring the problem design space of an asteroid rendezvous CubeSat mission. The validation of the tool was carried out using the NEA Scout asteroid and NEA Scout CubeSat mission requirements. The results demonstrate that the autonomous detection of small faint NEAs is achievable when the asteroid's positional uncertainty is within the CubeSat sensor's field of view. These findings have implications for current and future CubeSat missions to NEAs, offering insights into the feasibility of using off-the-shelf cameras for asteroid detection.

Keywords: CubeSat, Near-Earth Asteroid, Autonomous Detection, Camera Design

1. Introduction

In recent years, there has been a focus on developing technology for in-situ resource utilization on planetary bodies [1] [2]. Harnessing the solar system's natural resources is critical for future interplanetary human exploration and in-space manufacturing, as using the resources available in the immediate environment is easier and more cost-effective than bringing Earth-based resources into deep-space. Near-Earth Asteroids (NEAs) are resource-rich areas ready for extraction during deep-space missions and strategic plans from NASA have underlined the importance of characterizing such bodies [3]. Additionally, small NEAs (<50 m diameter), have been deemed high-priority scientific interest due to 1) the ease of capturing a smaller NEA to eventually return to Earth for further study and resource extraction and 2) smaller NEAs posing a danger of impacting Earth, especially those with low albedos which are less likely to be detected with Earth-based telescopes [4] [5] [3].

Low-cost flyby missions, e.g. CubeSats, can be sent to rendezvous with NEAs and further our understanding of these small bodies. Two recent CubeSat missions to characterize a <50 m NEA are NASA's Near-Earth Asteroid Scout (NEAScout) and ESA's Miniaturised - Asteroid Remote Geophysical Observer (M-ARGO) [6] [7] [8] [9]. While CubeSats' low-cost are a tremendous benefit to lower-priority science missions, enabling rapid exploration of the solar system with developing technologies, the drawback is the unavailability of cheaper space-rated equipment that are high performing like their high-cost counterparts. In the case of asteroid characterization and rendezvous missions, low-cost commercial-off-the-shelf (COTS) cameras can make the initial detection of the target asteroid difficult.

Due in part to the inability to fully characterize small NEAs from Earth, the positional uncertainty of a <50 m target asteroid is expected to be 10^3 km [10]. To ensure identification of the target asteroid with high positional uncertainty, the asteroid's $\pm 3\sigma$ positional uncertainty must be captured in the optical navigation imagery in the early approach phase [11]. [1] COTS cameras for CubeSats typically provide low field-of-view (FOV) [12]. This drives a requirement of detecting the asteroid from a distance of >60,000

[1] σ represents the standard deviation, indicating the variability of positions. A range of $\pm 3\sigma$ around the estimated position encompasses 99.7% of the data, assuming the distribution is normal, which ensures a high likelihood of capturing the asteroid despite its uncertain position.

km [4]. At that distance, a single image frame captured by a camera with a low FOV does not meet a signal detection requirement of signal-to-noise ratio (SNR) >7 [13].[2]

While the overall single-image SNR could be increased by a coordinated observational campaign to reduce the asteroid's positional uncertainty, increasing the size of the CubeSat to accommodate a larger aperture size, or changing the spacecraft approach trajectory, it is difficult to imagine a scenario in which a CubeSat camera could detect the target asteroid in a single image frame.

Given an interplanetary CubeSat's camera system and asteroid of interest, the detection (SNR >7) of the asteroid at a desirable distance during the approach phase, e.g. the distance where the asteroid's $\pm 3\sigma$ positional uncertainty fits within the sensor's FOV, may not be possible due to the CubeSat sensor's SNR being too low to guarantee a detection from a single image. This motivates the research question of how to bound the camera parameters and the required number of images to guarantee the autonomous detection of a small (<50 m diameter) faint (>20 absolute magnitude) NEA using a commercial off-the-shelf camera during the approach phase of an interplanetary CubeSat mission.

2. Prior Work

Previous NEA characterization or observation mission concepts have considered which optical imagers to use for asteroid detection [14] [15] [16] [17], but none have provided a robust analysis to generate mission camera requirements.

While some of these works consider the target asteroid's visual magnitude during camera selection [15] [16], they tend to choose a camera from a prior mission and neglect to consider the design space of their mission architecture. In fact, both [15] [17] recommend camera selection based on further analysis of the relative spacecraft and asteroid trajectories and asteroid parameters.

Sensitivity analysis of navigation on approach to a target asteroid has been performed by [18], but the work focuses on improving position accuracy measurements, instead of deriving camera requirements.

[2]A common detection threshold for NEAs is SNR > 5, but the authors include an additional buffer of 2 in their definition of signal detection.

This work's contribution is a tool to define camera characteristics based on apparent visual magnitude (and other physical characteristics) of the asteroid to improve a detection of the asteroid for a CubeSat asteroid rendezvous mission during approach phase. The tool also generates dwell time and limiting detectability based on fixed camera parameter inputs.

3. Methodology

3.1. Motivation

As previously, stated, it is expected that the single-frame SNR of the CubeSat's camera will be too low to guarantee a detection of the target asteroid ($<$50m diameter, $>$20 absolute magnitude). The technique to increase the SNR of an interplanetary CubeSat during its approach phase implements an autonomized version of ground-based observation techniques. Due to satellite jitter, CubeSat-based imagers are unable to use long exposure times to increase the SNR. One method to increase the SNR is to take many short exposure images and combine them with different techniques. In the shift-and-add technique, multiple images are stacked, with respect to the spacecraft's attitude, to synthetically boost the SNR [19].

While stacking subsequent frames increases the multi-frame SNR, the increase in SNR is not linear and depends instead on the square root of the number of stacked frames. This is due to the noise depending on the square root of the signal in the SNR. While the stacking technique is useful, it has diminishing returns with increasing stacked images, so it was not the only SNR augmentation technique used. This work considered the design of both the CubeSat camera and CubeSat orbit during the approach phase of a CubeSat mission in addition to the stacked frame technique to increase the single-frame SNR of a CubeSat detector.

As the single-frame SNR depends on the camera sensor and the observational configuration, it is important to develop a fast-prototyping tool which defines requirements at both the camera and trajectory design levels and explores the problem design space during the preliminary design phase. A standalone user-friendly design tool was created that considers the camera parameters, the asteroid parameters, the geometry of the approach phase and the increased SNR from the stacked frame technique to generate a synthetic SNR that meets the target asteroid detection requirements (SNR $\geq$7).

Table 1: Optional Camera and Asteroid Parameter Default Values

Wavelength Range	Optical Transmission	Mean Quantum Efficiency
497 - 583 nm	0.5	0.7

Spacecraft Positional Uncertainty	Asteroid Slope Parameter
1.5243e+06 m	0.15

3.2. Design Tool

An asteroid is considered to have been detected if the SNR is $\geq$7.

The standalone design tool uses both camera specifications and asteroid specifications as inputs. The camera parameters include the detector size, pixel size, field of view, aperture diameter and exposure time. The asteroid parameters include the asteroid positional uncertainty, the asteroid diameter, the absolute magnitude, the albedo and the phase angle.

Additional optional camera and asteroid parameters, that can be changed by the user, include the wavelength range of the response of the detector, optical transmission, mean quantum efficiency, the noise model of the camera and the spacecraft's positional uncertainty and the asteroid's slope parameter, respectively. The optional camera and asteroid parameters have default values based on a typical CubeSat mission in the design tool and can be found in Table 1.

To calculate the output synthetic SNR, the tool feeds the input parameters through four equations that govern the design space, as depicted in Figure 1. The four governing equations are: the optimal imaging range from the spacecraft camera to the asteroid, the apparent visual magnitude of the asteroid as seen from the spacecraft camera, the SNR of a single image frame, and the final synthetic SNR. The tool generates intermediate output plots for each equation output, which the designer uses to visually determine ranges of acceptable parameter inputs for the final desired SNR. There are four intermediate output plots, based on the design space equations. The four equations are derived in the next section.

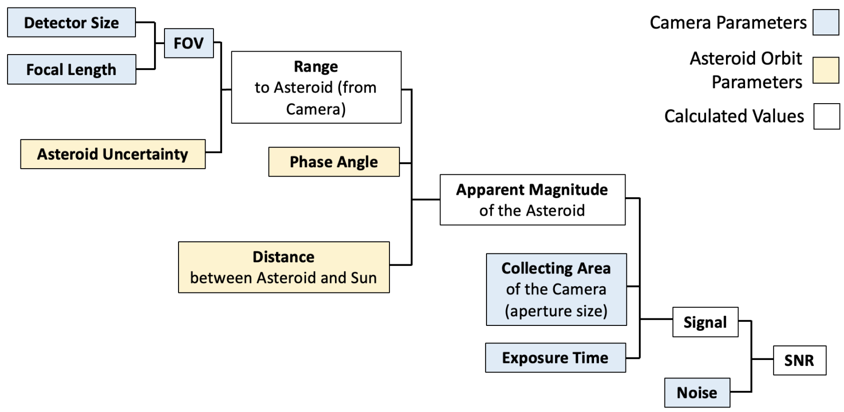

Figure 1: Flowchart of the design tool inputs and the four intermediate calculated values.

3.3. Design Tool Equations

3.3.1. Imaging Range from Spacecraft Camera to Target Asteroid

The optimum distance is defined as the range from the CubeSat to the asteroid where the FOV of the onboard camera encompasses the 2D-projected $\pm 3\sigma$ asteroid positional uncertainty ellipse, as seen in Figure 2. This is the closest distance from the spacecraft to the target asteroid which still guarantees with 99% $\pm 3\sigma$) confidence that the asteroid is captured within the FOV of the optical navigation imagery. A close approach is considered, instead of a further distance which would still include the 2D-projected $\pm 3\sigma$ asteroid positional uncertainty ellipse in the onboard camera's FOV, because more light from the target asteroid will be collected the closer the spacecraft is to the asteroid, thereby increasing the detection SNR.

To calculate the optimum distance for asteroid detection, the asteroid and spacecraft's positional uncertainties are considered as well as the camera's FOV. To calculate the distance, a simple trigonometric formula is used, where the uncertainty is the linear combination of the asteroid and spacecraft's positional uncertainty, as shown in Figure 2. A $\pm 3\sigma$ uncertainty is used to allow for enough time to refine the asteroid's ephemeris before using asteroid relative navigation and to allow for some small tangential relative velocity between the spacecraft and asteroid [11]. The equation for the optimum

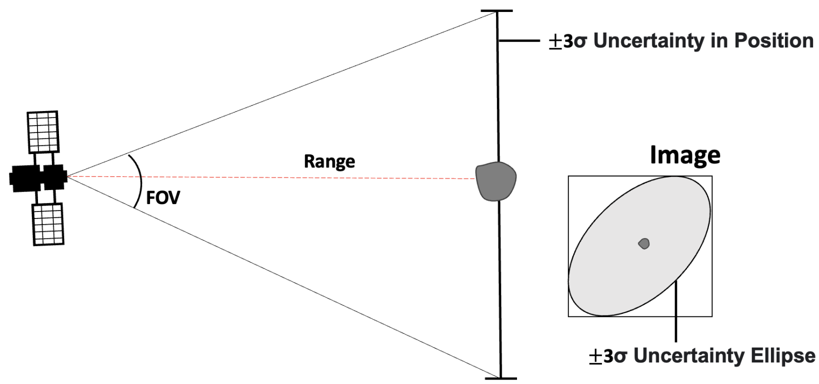

Figure 2: A diagram of the trigonometry between the asteroid and spacecraft when calculating the range needed for the FOV to include $\pm 3\sigma$ uncertainty in position.

range ρ is:

$$\rho = \frac{3\sigma}{\tan(FOV/2)} \tag{1}$$

3.3.2. Apparent Visual Magnitude of the Target Asteroid

The apparent visual magnitude of the target asteroid, as observed from the spacecraft camera, is the signal in a single-frame image. This work derives the apparent visual magnitude V from the absolute magnitude of the target asteroid H, the distance from the target asteroid to the Sun r, the distance from the target asteroid to the spacecraft camera Δ, and the phase angle α between the Sun, target asteroid and spacecraft camera, with the following equation:

$$V = H + 5\log_{10}(r\Delta) - 2.5\log_{10}[(1-G)\phi_1(\alpha) + G\phi_2(\alpha)], \tag{2}$$

where

$$\phi_1(\alpha) = e^{-A_1 \tan(\alpha/2)^{B_1}},$$
$$\phi_2(\alpha) = e^{-A_2 \tan(\alpha/2)^{B_2}},$$

and where G is the asteroid slope parameter and A_1=3.33, A_2=1.87, B_1=0.63, and B_2=1.22 are empirical values.
The derivation of the apparent magnitude equation can be found in [20].

3.3.3. SNR of a Single Image Frame and Final Synthetic SNR

There are two SNRs calculated in the tool; the first is the SNR of a single image frame, SNR, and the second is the synthetic SNR, SNR'. The SNR of a single image frame is calculated by the straightforward SNR equation:

$$\mathrm{SNR} = \frac{S}{N} \tag{3}$$

where S is signal and N is noise.

The signal is the light, or photon (particle) flux, received by the spacecraft camera from the asteroid. The signal includes the emitted particle flux of the asteroid $F_{\mathrm{asteroid,photon}}$. It is calculated by scaling a model [21] of the particle flux $F_{\mathrm{Vega,photon}}$ of the reference star Vega, by using the apparent magnitude of both Vega and the asteroid, m_v and m_a, respectively. This relationship is shown in the following equation [22]:

$$F_{asteroid,photon} = 10^{-0.4(m_a - m_v)} F_{Vega,photon}, \tag{4}$$

The absolute magnitude of the asteroid of interest can be found using the Minor Planet Center Database [23]. Vega's apparent magnitude is 0.003 and can be approximated as zero. These values are used to calculate the emitting signal of the asteroid.

The signal received by the spacecraft camera F_{camera} is the emitted signal of the asteroid $F_{\mathrm{asteroid,photon}}$ scaled by the area of the collector (aperture diameter) A, the exposure time t, the camera mean quantum efficiency η, and optical transmission ε:

$$F_{camera} = F_{asteroid,photon}\ A\ t\ \eta\ \varepsilon. \tag{5}$$

This equation represents the signal of a single-frame image.

The noise model includes the noise generated from the camera (read-out noise, quantization noise, pixel response non-uniformity noise, dark current noise and fixed pattern noise) and the background image noise. A derivation of the noise model and noise values used in equation (3) can be found in [21].

Combining the output of the signal and noise derivations, the single-frame SNR used in the design tool is represented by:

$$\mathrm{SNR} = \frac{F_{camera}}{N}. \tag{6}$$

SNR', the final synthetic SNR, is generated by stacking n individual frames and is calculated by:

$$SNR' = SNR\sqrt{n} \tag{7}$$

4. Design Tool Plots

The four governing design tool equations, (1)(2)(6)(7), derived in the previous section, are shown as the four output plots in the design tool. The plots provide a visual representation of the CubeSat mission design space and help the user choose both camera and approach orbit parameter specifications.

Each plot's equation is represented by contour lines, with the equation's inputs represented on the axes. The first plot, Figure 3, depicts the optimal imaging range equation (1) as a function of the spacecraft camera's FOV and the linear addition of both the spacecraft and asteroid's positional uncertainties. As the FOV of the spacecraft's camera increases, the optimal range decreases, and as the total positional uncertainty increases, the optimal range increases. Intuitively, as the area the camera observes increases, the camera can capture the total area of a constant uncertainty ellipse at closer distances to the asteroid, and conversely, as the uncertainty ellipse increases in size, a constant FOV of a camera will need to be positioned further away to encompass the ellipse.

The second design tool plot, Figure 4, depicts the visual magnitude of the target asteroid, calculated using equation (2), as a function of the phase angle of the spacecraft on approach to the asteroid and the previously calculated optimal range to the asteroid. As the phase angle increases, the visual magnitude increases and as the range to the asteroid increases, the visual magnitude also increases. Note that the magnitude of a celestial body appears brighter at lower values. It follows that as the phase angle increases, or the angle from which the asteroid is illuminated by the sun, as seen by the spacecraft, it moves farther from the fully illuminated designation (0 degrees), and the asteroid will appear less bright. The same scenario occurs as the spacecraft moves further from the asteroid—the further an observer is from a source of light, the dimmer it will appear.

The third design tool plot, Figure 5, depicts the single-frame SNR, calculated using equation (6), of the spacecraft camera as a function of the collecting area of the camera times the exposure time and the visual magnitude of the asteroid. As the camera parameters (collecting area and/or exposure

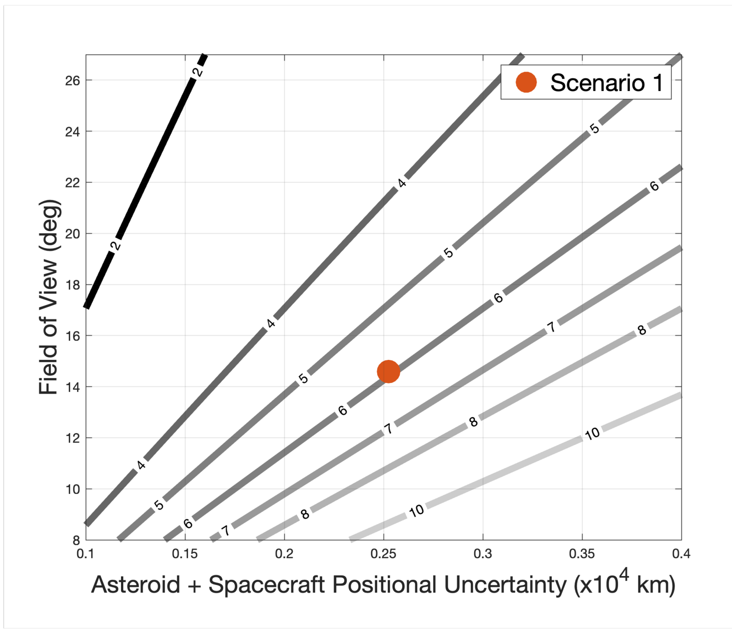

Figure 3: A plot with contours depicting the optimal range from the spacecraft, calculated using equation (1), to the asteroid in units of 10^4 km as a function of field of view in units of degrees and the combination of the asteroid and camera positional uncertainties in units of 10^4 km. The red circle indicates the range calculated with the user's input field of view and positional uncertainties.

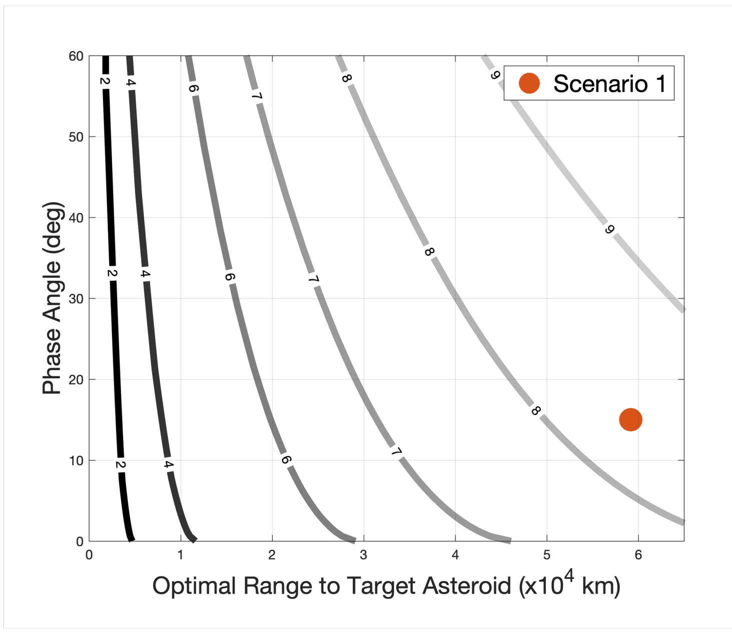

Figure 4: A plot with contours depicting the apparent visual magnitude of the target, calculated using (2), asteroid as a function of phase angle in units of degrees and the range to the asteroid in units of 10^4 kilometers. The red circle represents the visual magnitude from the user input phase angle and calculated range to the asteroid.

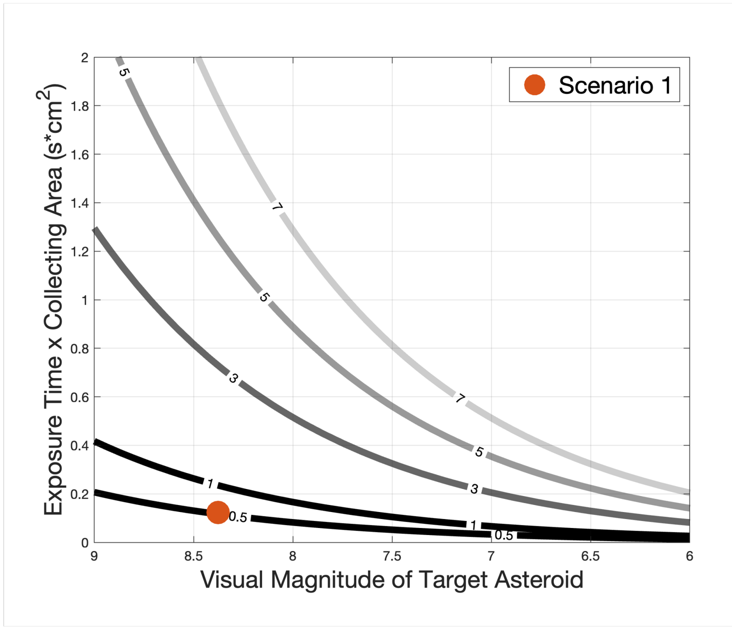

Figure 5: A plot with contours depicting the SNR received by the spacecraft camera, calculated using (6), as a function of the product of the exposure time and collecting area of the camera and as a function of visual magnitude. The red circle represents the single-frame SNR from the user input camera parameters and calculated visual magnitude.

time) increase, the SNR increases and as the visual magnitude decreases, the SNR also increases. Intuitively, as more light is collected in a bigger area and over a longer period of time, the signal will also increase, leading to a larger SNR. As the visual magnitude decreases (as the asteroid appears brighter) more signal is received and so the SNR again increases. The vertical axis is the product of exposure time and collecting area to include more camera parameters in the single-frame SNR plot.

The fourth plot, Figure 6, shows the final synthetic SNR, SNR', as a function of the single-frame SNR and the number of stacked frames, as derived in equation (7). The SNR' plot depicts the number of stacked frames with the single-frame SNR required to generate a final synthetic SNR of 7. In Fig. 6, a single-frame SNR of $\sim$0.5 requires $\sim$200 stacked frames in order to obtain a final synthetic SNR of 7.

These four output plots, from the four equations governing the final synthetic SNR, are used to show the design tool user how small changes in a system parameter in an early equation can cascade into bigger changes at the

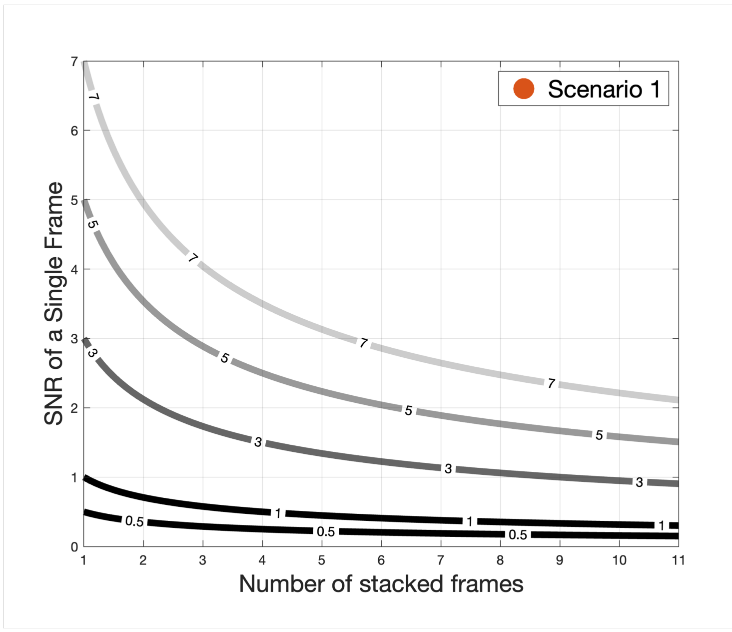

Figure 6: A plot with contours depicting the final synthetic SNR, calculated using (7), as a function of the single-frame SNR and the number of stacked frames. The red circle represents a final synthetic SNR of 7 from the calculated single-frame SNR and the required number of stacked frames.

final synthetic SNR. The red circle on each of the plots serves as a benchmark of the current capabilities of the chosen modeled system. Additional circles can be included in the plots to represent user changes in different design tool parameters, as shown in the following section. When used together, the four plots form a useful waterfall effect of the mission design parameters on the final synthetic SNR.

5. Asteroid 2014 YD Results for M-ARGO

To demonstrate the ability of the design tool, the ESA CubeSat mission to characterize a <50m NEA, Miniaturised - Asteroid Remote Geophysical Observer (M-ARGO), is used as an example mission. Previous work identified near-earth asteroid 2014 YD as a potential target for the M-ARGO mission [12] [9] and is used as the target asteroid in the following design tool demonstration.

First, the proposed navigation camera for the M-ARGO mission is considered for initial mission parameters, then the design tool improves the final synthetic SNR to ≥ 7 while simultaneously generating the requirements for both camera hardware and the spacecraft orbit approach. Four different scenarios of iterative parameter selections are considered as the design space is explored.

The asteroid 2014 YD parameters were generated using the JPL Horizon System and the Minor Planet Center dataset [24] [23]. Table 2 compiles the asteroid parameter values used in the design tool for target asteroid 2014 YD. Prior work also identified potential cameras for use in the M-ARGO mission [12]. Table 3 lists the two different image sensors (CMV4000 and FaintStar) considered from the sensor datasheets [25] [26].

The first scenario, represented by a red circle (Fig. 7), uses the proposed M-ARGO camera (Table 2 FaintStar). The FaintStar camera provides conservative parameters of a CubeSat camera. A single-frame SNR of 0.5 is generated using the conservative input parameters (Fig. 7), which is not high enough to guarantee a detection of the asteroid, even with the stacked frame technique, as stacking an SNR less than 1 will always result in noise larger than signal. However, even considering using the stacked frame technique, it will take 200 stacked frames to reach a synthetic SNR of 7. This number of stacked frames is unrealistic for the onboard processing capacity of a CubeSat, where the maximum number of stacked frames can be realistically estimated on the order of magnitude of 10 frames [10].

In the following scenarios, the tool will be used to change mission parameters to improve the detection of the target asteroid.

In the second scenario, the exposure time is considered and is increased from 0.1 seconds to 1.0 second. Figure 7 shows the initial parameters from scenario 1 as a red circle and the new parameters in scenario 2 with a green circle. The two scenarios both return the same range and visual magnitude values but diverge in the later SNR plots (Fig. 7). In the single-frame SNR plot, the scenario 1 parameters return a single-frame SNR of 0.5 while scenario 2, with the increased exposure time, returns a single-frame SNR of 5.3. While the increased exposure time in scenario 2 results in a higher single-frame SNR, an SNR of ≥ 7 is needed to meet mission requirements. Using the stacking frame technique, a synthetic SNR of 7.2 is returned after two stacked frames, fulfilling the mission requirements for the threshold SNR.

However, another mission consideration for an interplanetary CubeSat mission is the low positioning accuracy. The exposure time is reduced from 1.0 second to 0.1 seconds to compensate for blur from spacecraft jitter. The tool can now be used to change a different mission parameter instead of exposure time to still guarantee the asteroid detection.

The third scenario, represented by a blue circle (Fig. 7), uses the CMV4000 sensor (Table 3), which increases the sensor size, and doubles the aperture diameter while keeping the other parameters the same. The single-frame SNR is 2.5, requiring 8 stacked frames to generate a synthetic SNR of 7.

In the fourth scenario, represented by a purple circle (Fig. 7), the asteroid orbit parameters are changed, decreasing the range to half of the optimum range to the asteroid and decreasing the phase angle from 15 degrees to 10 degrees while the camera parameters are held constant, using the original conservative camera (Table 3 FaintStar). Because of the decreased range to the asteroid, the FOV of the camera no longer encompasses the $\pm 3\sigma$ positional uncertainty of the asteroid. This requirement could still be met by utilizing the scanning technique, where the camera captures four images in a square 'scanning' format to simulate the same coverage of the camera's FOV at the optimum range. The result of using the scanning technique is a single frame SNR of 2.5, which, like the prior scenario, requires 8 stacked frames to return a final synthetic SNR of 7. However, this approach is limited by the pointing error of the spacecraft and the processing power onboard, as 24 images would be generated and processed.

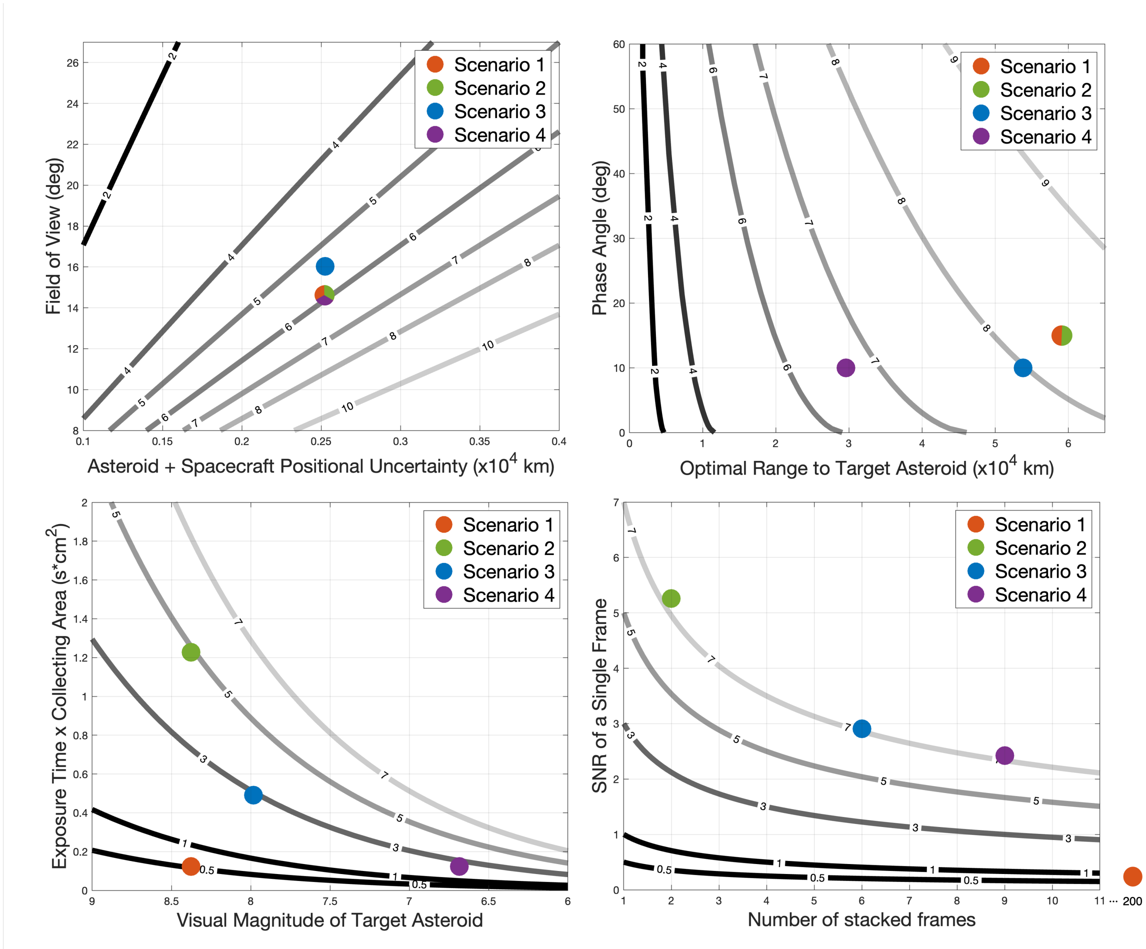

Figure 7: Design tool output of scenarios 1 (red circle), 2 (green circle), 3 (blue circle) and 4 (purple circle). Overlapping colors represent matching parameters between scenarios.

Table 2: Asteroid Parameter Values for 2014 YD and 2020 GE

Parameter	Asteroid 2014 YD	Asteroid 2020 GE
Asteroid Positional Uncertainty	1,524.3 km	50 km
Spacecraft Positional Uncertainty	1,000 km	1,000 km
Asteroid Diameter	47 m	18 m
Absolute Magnitude	24.3	28.2
Albedo	0.15	0.15
Distance from the Sun to the Asteroid	1.1261 AU	1.05 AU
Phase Angle	15 deg	15 deg

Table 3: Parameter Values of the Cameras

Parameter	CMV4000	FaintStar	NEA Scout Camera
Image Size	2048 x 2048 pixels	1024 x 1024 pixels	3840 x 3840 pixels
Pixel Size	5.5 microns	10 microns	6.4 microns
Focal Length	40 mm	40 mm	52 mm
Aperture Diameter	25 mm	12.5 mm	18.6 mm
Field of View	16 deg	8 deg	27 deg
Exposure Time	0.1 s	0.1 s	0.7 s
Optical Transmission	0.5	0.5	0.5
Wavelength Range	497nm to 583nm	497nm to 583nm	497nm to 583nm

6. Validating the Design Tool

In this section, the design tool is validated with published NEA Scout parameters.[3]

6.1. Asteroid 2020 GE Results for NEA Scout

NEA Scout mission's asteroid target, 2020 GE, was reported by the NASA JPL press release in January of 2022 [28]. Three additional papers published on NEA Scout have been utilized in determining the camera (Table 3 NEA Scout Camera) and asteroid approach parameters (Table 2 Asteroid 2020 GE) [11] [4] [10].

The asteroid positional uncertainty was generated with the JPL horizon system tool ($\sigma = 50$ km) and the phase angle was kept the same as previous analyses at 15 degrees [24]. Figure 8 shows the results of the design tool. The optimal range to the asteroid is 12,500km, and with the NEA Scout camera parameters an SNR of 5.7 is returned, requiring only two stacked images to return an SNR of 7. The tool's output matches the requirements of the NEA Scout mission with a number of required stacked frames (n=2) below the onboard memory capacity of n=5 [10], with the $\pm 3\sigma$ positional uncertainty of the asteroid captured in the camera's FOV (completed with the optimal range calculation) and a phase angle $<$ 50 degrees [11], validating the results of our model.

[3]Note that although NEA Scout was not successfully deployed [27], the authors still use the published NEA Scout parameters for validation.

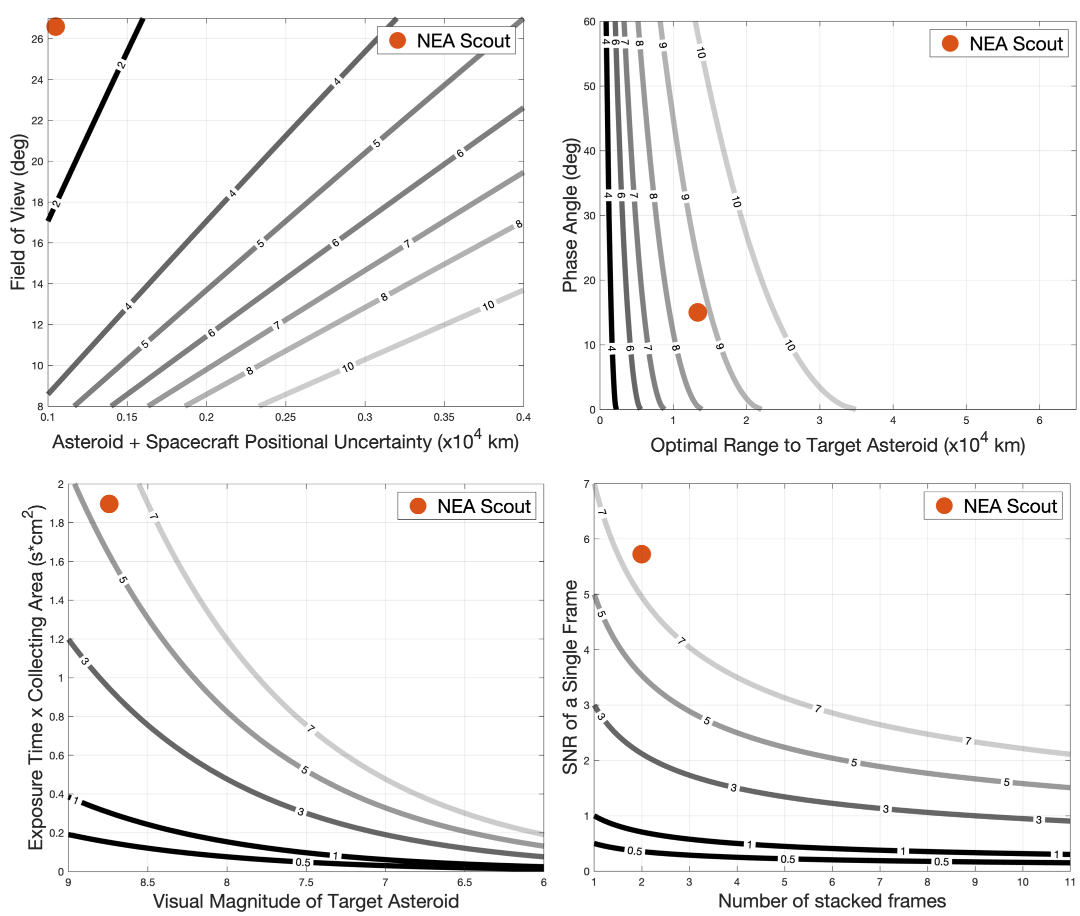

Figure 8: Design tool output with NEA Scout mission parameters (red circle).

6.2. Conclusions

This work developed a design tool that provides asteroid rendezvous CubeSat mission designers both onboard camera and spacecraft orbit requirements to ensure asteroid detection during the approach phase of the mission. Values for both the CubeSat navigation system parameters and asteroid orbit parameters are produced by the tool in which the detection of the asteroid is guaranteed when the $\pm 3\sigma$ of the asteroid's positional uncertainty is included in the FOV of the CubeSat sensor. The design tool provides the user with output camera hardware specifications, approach orbit, range requirements, and the number of stacked frames necessary for an SNR ≥ 7 for an asteroid rendezvous CubeSat mission design.

The results were validated with a second asteroid irradiance model [21] to ensure the accuracy of the collected particle flux and the NEA Scout asteroid and the published NEA Scout CubeSat mission requirements to verify the range and synthetic SNR outputs.

This work has demonstrated how the design tool can explore the design space of the detection of the asteroid in a single frame by increasing the synthetic SNR when the $\pm 3\sigma$ of the asteroid's positional uncertainty is included in the FOV of the CubeSat sensor and has implications for current and future CubeSat missions to NEAs. Another application area for the design tool would be increasing the likelihood of detecting NEAs from cis-lunar space, for example, characterizing a space-based telescope for an early-warning asteroid system.

7. Acknowledgement

This work was supported by the GEM Fellowship and the Fratelli Roberto ed Agostino Rocca Foundation.

References

[1] N.A., NASA's Moon to Mars Strategy and Objectives Development, Tech. Rep. NP-2023-03-3115-HQ, NASA Headquarters Washington, DC 20546 (2023).

[2] N.A., NASA Strategic Plan 2022, Tech. Rep. NPD 1001.0D, NASA Headquarters Washington, DC 20546 (2022).

[3] N.A., NASA Strategic Plan 2014, Tech. Rep. NP-2014-01-964-HQ, NASA Headquarters Washington, DC 20546 (2014).

[4] J. Lightholder, D. R. Thompson, J. Castillo-Rogez, C. Basset, Near earth asteroid scout cubesat science data retrieval optimization using onboard data analysis, in: 2019 IEEE Aerospace Conference, 2019. doi:10.110/AERO.2019.8742190.

[5] NASA Planetary Defense Strategy I& Action Plan Working Group, NASA Planetary Defense Strategy and Action Plan, Tech. Rep. NP-2023-04-3120-HQ, NASA Headquarters Washington, DC 20546 (2023).

[6] L. McNutt, L. Johnson, P. Kahn, J. Castillo-Rogez, A. Frick, Near-Earth Asteroid (NEA) Scout, in: AIAA SPACE 2014 Conference and Exposition. doi:10.2514/6.2014-4435.

[7] T. R. Lockett, J. Castillo-Rogez, L. Johnson, J. Matus, J. Lightholder, A. Marinan, A. Few, Near-earth asteroid scout flight mission, IEEE Aerospace and Electronic Systems Magazine 35 (3) (2020) 20–29. doi:10.1109/MAES.2019.2958729.

[8] R. Walker and D. Koschny and C. Bramanti and I. Carnelli and ESA CDF Study Team, Miniaturised Asteroid Remote Geophysical Observer (M-ARGO): a stand-alone deep space CubeSat system for low-cost science and exploration missions, in: 6th Interplanetary CubeSat Workshop, 2017.

[9] F. Topputo, Y. Wang, C. Giordano, V. Franzese, H. Goldberg, F. Perez-Lissi, R. Walker, Envelop of reachable asteroids by m-argo cubesat, Advances in Space Research 67 (12) (2021) 4193–4221. doi:https://doi.org/10.1016/j.asr.2021.02.031.

[10] W. Huffman, D. R. Thompson, B. Bue, J. Castillo-Rogez, J. Boland, Autonomous Onboard Point Source Detection by Small Exploration Spacecraft, Publications of the Astronomical Society of the Pacific 127 (958) (2015) 1279. doi:10.1086/684172.

[11] T. R. Lockett, J. Castillo-Rogez, L. Johnson, J. Matus, J. Lightholder, A. Marinan, A. Few, Near-earth asteroid scout flight mission, IEEE Aerospace and Electronic Systems Magazine 35 (3) (2020) 20–29. doi:10.1109/MAES.2019.2958729.

[12] V. Franzese, Autonomous navigation for interplanetary cubesats at different scales, Ph.D. thesis, Via La Masa, 34, 20156, Milano, Italy (2021).

[13] M. Shao, B. Nemati, C. Zhai, S. G. Turyshev, J. Sandhu, G. Hallinan, L. K. Harding, Finding very small near-earth asteroids using synthetic tracking, The Astrophysical Journal 782 (1) (2014) 1. doi:10.1088/0004-637X/782/1/1.

[14] S. Casini, I. Fodde, B. Monna, A. Cervone, E. Gill, Novel 3u standalone cubesat architecture for autonomous near earth asteroid fly-by, Aerospace 8 (1) (2021). doi:10.3390/aerospace8010009.

[15] P. Machuca, J.-P. Sánchez, S. Greenland, Asteroid flyby opportunities using semi-autonomous cubesats: Mission design and science opportunities, Planetary and Space Science (11 2018). doi:10.1016/j.pss.2018.11.002.

[16] T. Ikenaga, Y. Sugimoto, M. Ceriotti, M. Yoshikawa, T. Yanagisawa, H. Ikeda, N. Ishii, T. Ito, M. Utashima, A concept of hazardous neo detection and impact warning system, Acta Astronautica 156 (2019) 284–296. doi:https://doi.org/10.1016/j.actaastro.2018.06.058.

[17] D. Mages, D. Landau, B. Donitz, S. Bhaskaran, Navigation evaluation for fast interstellar object flybys, Acta Astronautica 191 (2022) 359–373. doi:https://doi.org/10.1016/j.actaastro.2021.11.012.

[18] K. Dennison, S. D'Amico, Multi-agent stereovision sensitivity analysis for rendezvous with non-cooperative targets, in: 3rd Space Imaging Workshop, 2023.
URL https://seal.ae.gatech.edu/sites/default/files/2022-10/SIW22-04.pdf

[19] T. Yanagisawa, A. Nakajima, K.-i. Kadota, H. Kurosaki, T. Nakamura, F. Yoshida, B. Dermawan, Y. Sato, Automatic Detection Algorithm for Small Moving Objects, Publications of the Astronomical Society of Japan 57 (2) (2005) 399–408. doi:10.1093/pasj/57.2.399.

[20] E. Bowell, B. Hapke, D. Domingue, K. Lumme, J. Peltoniemi, A. W. Harris, Application of photometric models to asteroids., in: R. P. Binzel, T. Gehrels, M. S. Matthews (Eds.), Asteroids II, 1989, pp. 524–556.

[21] V. Franzese, F. Topputo, Celestial bodies far-range detection with deep-space cubesats, Sensors 23 (9) (2023). doi:10.3390/s23094544.

[22] N. Pogson, Magnitudes of Thirty-six of the Minor Planets for the First Day of each Month of the Year 1857, Monthly Notices of the Royal Astronomical Society 17 (1) (1856) 12–15. doi:10.1093/mnras/17.1.12.

[23] G. Williams, S. Keys, M. Rudenko, J. Galache, Minor planet center - asteroid orbital data, VO resource provided by the GAVO Data Center (2009).
URL https://dc.zah.uni-heidelberg.de/mpc/q/pla/info,Retrieved:(2022/05/1)

[24] N. A., JPL Horizons System.
URL https://ssd.jpl.nasa.gov/horizons/app.html#/,Retrieved:(2022/05/1)

[25] N. A., CMV4000: Global Shutter CMOS Image Sensor for Machine Vision, ams-OSRAM AG, Tobelbader Strasse 30 8141 Premstaetten Austria, Europe (Jan 2023).

[26] W. Ogiers, K. Ruythooren, K. V. Wichelen, M. Dendoncker, S. Kowaltschek, B. Razgus, Faintstar: an intelligent single-chip sensor head for star trackers—prototype results 10 (2018) 605–619. doi:https://doi.org/10.1007/s12567-018-0220-x.

[27] K. Chang, Small explorers hitched a ride to space with Artemis I, The New York TimesPublished Electronically (Nov. 2022).

[28] N. A., NASA Solar Sail Mission to Chase Tiny Asteroid After Artemis I Launch (Jan 2022).
URL https://www.jpl.nasa.gov/news/nasa-solar-sail-mission-to-chase-tiny-asteroid-after-artemis-i-launch,Retrieved:(2022/05/1)